

Microstructure and superconducting properties of Sn-In and Sn-In-Bi alloys as Pb-free superconducting solders

T Mousavi, C Aksoy, CRM Grovenor, SC Speller

Materials Department, Oxford University, Oxford, OX1 3PH, UK

Abstract

In this work the microstructure and superconducting properties of various compositions of binary Sn-In and ternary Sn-In-Bi alloys have been studied as potential replacements for the Pb-based superconducting solders currently used for superconducting joints between technological low temperature superconducting wires. The influence of chemistry and microstructure on the superconducting properties are investigated. Both the Sn-In β and γ phases are stable over a fairly wide range of chemical composition, with the superconducting properties of each phase improving with increasing solute concentration, but the results show that the In-rich β phase has better superconducting properties than the Sn-rich γ phase. For this reason, in both the binary Sn-In and the ternary Sn-In-Bi systems, the best superconducting properties are achieved in alloys with a high volume fraction of β -phase. The ternary alloys generally show better superconducting properties than the binary alloys, with the highest values of 6.9 K, 0.18 T and 1.3×10^8 A/m² measured for T_C , B_{C2} (at 4.2 K) and J_C (at 4.2 K, 0.01 T) respectively in the $\text{Sn}_{35}\text{In}_{50}\text{Bi}_{15}$ alloy that consists of a matrix of β -phase with fine fibres of γ and BiIn_2 . The dependence of the pinning force on the reduced magnetic field exhibits a scaling law behaviour with the maximum at $B/B_{C2} \sim 0.2$ indicating that the dominant mechanism is surface normal pinning in these solders. Rapid solidification in liquid nitrogen results in manipulation of the phase chemistry by both increasing the solute content in the majority phase, changing the fraction of each phase and reducing the scale of the microstructure, leading to significant improvements in superconducting performance. However, the quenched alloys age

considerably, even at room temperature, resulting in a deterioration in B_{C2} and J_C values over a few days.

Keywords: Superconducting joints, Pb-free solders, microstructure, pinning mechanism.

1. Introduction

Persistent current joints are a critical component of commercial superconducting magnets. The standard jointing method widely used in the magnet industry for technological low temperature superconducting wires such as NbTi and Nb₃Sn wires uses a superconducting solder (e.g. PbBi) [1-5]. In these joints the physical and superconducting properties of the solder materials inevitably play an important role in the overall performance of the joint. Key requirements for superconducting solders include low melting point to prevent degradation of the superconducting filaments during joining, good wettability of the superconducting filaments, suitable liquid phase viscosity, and finally adequate superconducting properties to enable sufficient supercurrent to pass through the joint under typical operating conditions (typically at 4.2K in a field of 1 T for an MRI magnet). The microstructure of the solders also strongly influences the overall performance of the joints, both in terms of superconducting properties and other important physical/mechanical properties [6]. In a multi-phase alloy, the superconducting transition temperature (T_C) and upper critical field (B_{C2}) are dominated by the intrinsic properties of the majority phase. However, the critical current density (J_C) under operational conditions will be influenced by both the intrinsic properties of the majority phase and the flux pinning landscape provided by the microstructure including grain boundaries, interphase boundaries and other structural defects [6; 7].

The requirement for low melting points means that superconducting solder systems are normally eutectic alloys with at least two phase microstructures, and with at least the majority

phase being superconducting. Some of the alloys which were studied in the 1900s and 2000s as superconducting solders include Pb-Bi [6], Sn-Pb [6; 8], Sn-In [6; 8; 9], In-Pb [7; 8], In-Bi [6], Pb-Bi-Sn [1; 2; 4; 8], Sn-Pb-Cd [8] and Sn-Bi [8], as reviewed in [10]. Of these systems, the most popular superconducting solders are the PbBi alloys commonly used in industry to join both NbTi and Nb₃Sn conductors [1-3; 11; 12]. In addition to having a low melting point (120°C), PbBi joints are capable of carrying 1000 A at 4.2 K in 1 T field, with ultra-low resistances in the range 10^{-13} – 10^{-14} Ω [3] making them suitable for persistent mode joints in commercial magnets. However, new restrictions on the commercial use of Pb [13; 14] necessitate the development of replacement Pb-free solder materials with good J_C and B_{C2} values. In this work, we have studied the binary Sn-In and ternary Sn-In-Bi systems as potential replacements for Pb-based alloys. The relation between microstructure, composition and superconducting properties in these two systems is investigated to optimise the superconducting properties. The dominant pinning mechanisms and the effects of quench and ageing processes on the properties and stability of the solders have also been studied.

2. Experimental methods

Binary Sn-In and ternary Sn-In-Bi alloys with a range of compositions (listed in Table 1) were fabricated by melting pure tin, indium and bismuth at temperatures up to 300°C on a hot-plate. Cylindrical samples with a diameter of 2 mm were cast using a pipette attachment to suck the molten alloy into heated cylindrical quartz tubes. The samples were either allowed to cool in air or were solidified at a much faster rate (quenched) by immersion of the quartz tube containing the molten alloy into a bath of liquid nitrogen.

Microstructural characterization was carried out using analytical scanning electron microscopy (SEM). A Zeiss Merlin SEM with an Oxford Instruments (OI) 150mm² XMax EDX detector was used at relatively low voltage (10kV) to perform high resolution chemical analysis. Lower

spatial resolution maps were obtained using a JEOL 5510 SEM with OI SDD detector operating at 20kV accelerating voltage. OI Aztec software was used to generate phase maps, choosing the parameters for partitioning into separate phases carefully to prevent anomalous results. The average compositions of each phase were calculated from spectra reconstructed from each phase in the map. An estimate of the interphase boundary length per unit area for the majority phase in each microstructure was calculated from the phase-map images in MATLAB, using a procedure involving the “bwboundaries” function to identify the boundaries. Electron Backscatter Diffraction Analysis (EBSD) was carried out on a Zeiss Evo SEM equipped with a Bruker EBSD camera and Espirit 1.9 software. X-ray diffraction (XRD) analysis was carried out using Cu Ka radiation in a Philips θ – 2θ diffractometer. Superconducting properties were measured using a Quantum Design SQUID magnetometer. M-T curves were taken in a small measurement field of 0.01T to determine the T_C , and B_{C2} and J_C values were extracted from full hysteresis curves taken at a range of selected temperatures. For these measurements, all the samples were prepared with the same size and shape (cylinders with 2 mm diameter and 2.5 mm in length) and were carefully aligned with their axis parallel to the applied magnetic field. To extract J_C from magnetic hysteresis loops, Bean’s model and self-field corrections were applied [15]. To study the scaling law and pinning mechanism using Kramer plots (pinning force density versus reduced magnetic field) [16], the Dew-Hughes model [17] and multi-elementary scaling law [18] were applied.

Table 1: The composition of various alloys studied in this work.

Sample label Content	B1	B2	B3	B4	B5	T1	T2	T3	T4
In (wt%)	80	65	55	35	20	50	30	50	65
Sn (wt%)	20	35	45	65	80	20	50	35	5
Bi (wt%)	-	-	-	-	-	30	20	15	30

3. Results and Discussion

3.1. Sn-In Binary system

Figure 1 shows the five different binary alloy compositions studied in this work on a calculated Sn-In phase diagram [19]. EDX phase maps of the five air-cooled binary Sn-In alloys are presented in Figure 2. Sample B1 (with the lowest concentration of Sn) is found, as expected, to be single phase β . In samples B2, B3 and B4 with higher Sn content, two-phase ($\beta + \gamma$) microstructures are found, with the area fraction of the Sn-rich γ phase increasing with increasing Sn content, also consistent with the phase diagram. Increasing the Sn content further (B5) results in the formation of single phase γ . XRD data has also confirmed the presence of similar phases in these samples.

In spite of a similar cooling rate for all the samples (air cooling from the same melt temperature), the scale of the two-phase microstructure is different in these alloys. From the phase diagram, it is expected that sample B2 should initially solidify as the β phase, with a precipitation reaction occurring at lower temperature as the solid solubility of Sn in β reduces, producing small isolated islands of γ phase within the β matrix. This precipitation reaction can occur even during the relatively rapid air-cooling of the sample because the solid state diffusion

rate is very high in these low melting point systems. Sample B3 also shows a relatively fine scale microstructure resulting from the majority of the alloy solidifying by the eutectic transformation ($L \rightarrow \beta + \gamma$), but we note that the observed volume fractions of the two phases of about 50% β and 50% γ correspond to values we would predict from the phase diagram at room temperature rather than at the eutectic temperature, again highlighting that solid state diffusion in these alloys is fast. In contrast, sample B4 shows a considerably larger microstructure. In this case, a large volume fraction of primary γ phase grows first over a range of temperatures, with the final liquid transforming by the eutectic reaction to $\beta + \gamma$. As solid state diffusion is so rapid, the primary γ phase in the final microstructure cannot easily be distinguished from that formed in the eutectic reaction.

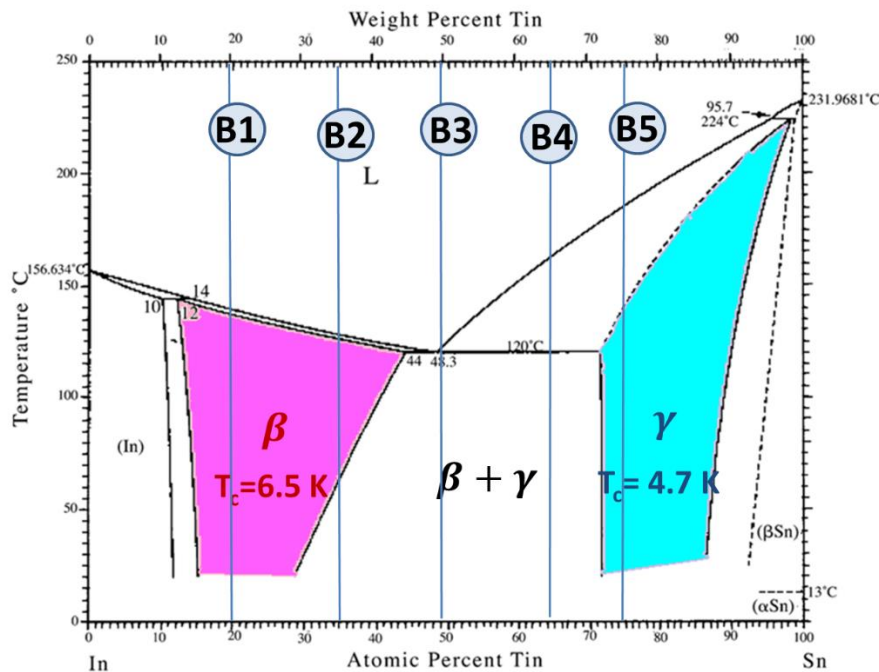


Figure 1: Calculated Sn-In phase diagram [19] with the alloy compositions (B1-B5) studied in this work.

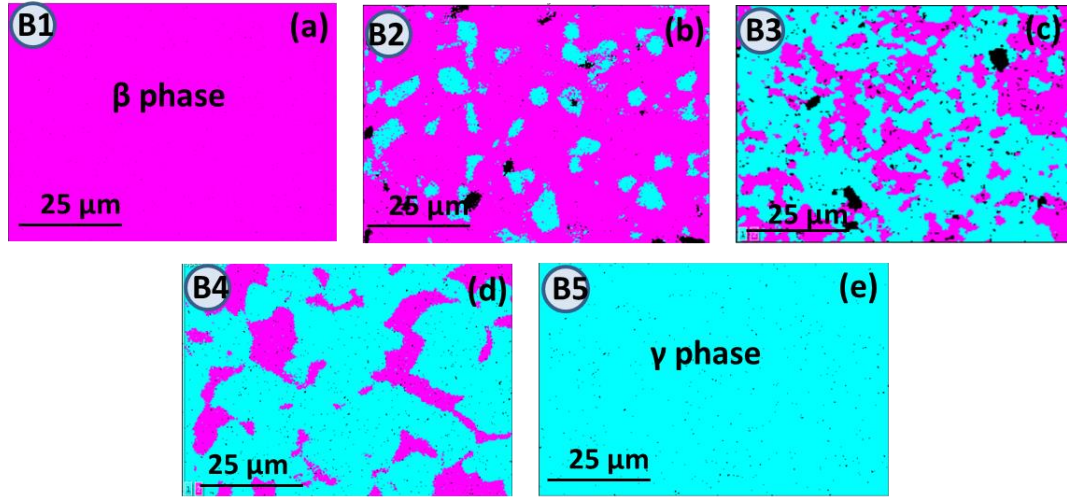


Figure 2: (a-e) Phase maps of the five binary Sn-In alloys (B1-B5). The pink and blue regions represent the β phase and γ phase respectively.

Superconducting properties of the binary alloys are shown in Figure 3. All the alloys show transition temperatures (T_C) above 4.2 K in low measurement field of 10 Oe. By comparing the B1 and B5 samples which are pure In-rich β and Sn-rich γ phases respectively, it can be seen that the β -phase has better superconducting properties (higher T_C , B_{C2} and J_C values). For the β -phase these values are 5.9 K, 0.066 T (at 4.2 K) and $6.1 \times 10^7 \text{ A/m}^2$ (at 0.01 T, 4.2 K), and for the γ -phase these values are 4.5 K, 0.025 T (at 4.2 K) and $1.22 \times 10^7 \text{ A/m}^2$ (at 0.01 T, 4.2 K). Among these samples, the best superconducting properties were measured for sample B2 which contains the β -phase as the majority phase with a small fraction of the γ -phase dispersed on a relatively fine scale (Figure 3b).

According to the Sn-In binary phase diagram, the β and γ phases are stable over a relatively wide range of composition, and because we have precise information on the phase chemistry in our samples we can correlate this data with the superconducting properties of each phase individually. As shown in Figure 4a and b, the T_C and B_{C2} values of both the In-rich β phase and the Sn-rich γ phase improve with increasing solute content of Sn and In respectively.

When the microstructure of the sample includes both phases (e.g. in samples B2, B3 and B4), one phase is usually present at a large volume fraction and forms a continuous matrix containing the other disconnected phase. In samples with this kind of microstructure, it has been reported that the overall superconducting properties of the alloy is usually controlled by those of the dominant superconducting phase [20]. Since the β phase has better superconducting properties than the γ phase, it is not surprising that the T_C and B_{C2} values increase as we increase the volume fraction of the In-rich β -phase, as shown in Figure 4c. In this diagram, sample B2 which contains a majority of β phase exhibits the best superconducting properties even better than those of the pure β -phase sample (B1). This can be attributed to the β -phase being saturated in Sn. Increasing the overall Sn content in the alloy further (sample B3 and B4) does not change the chemical composition of this β phase, but increases the volume fraction of the γ phase. Since the γ phase has inferior superconducting properties, this explains why alloy B2 exhibits the best superconducting performance.

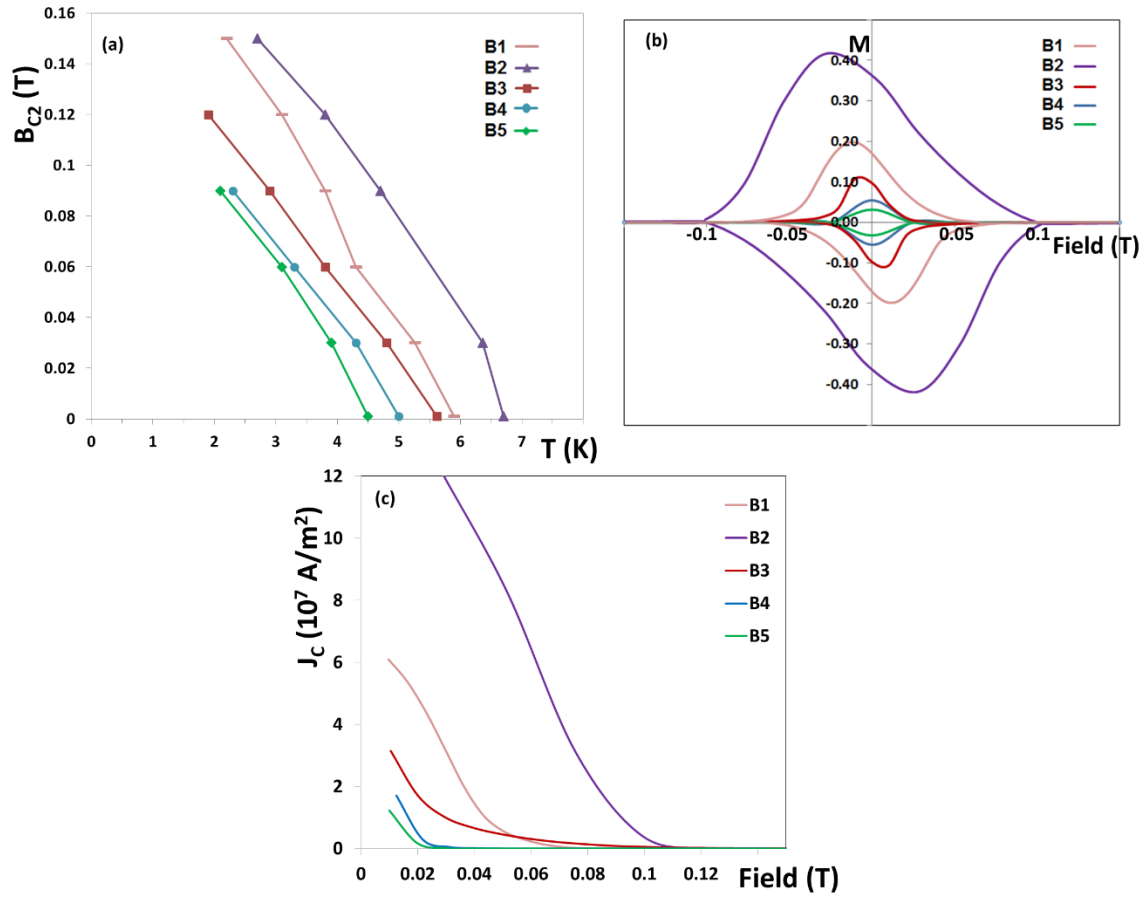


Figure 3: (a) B_{C2} as a function of temperature (each data point in the graph is transition temperature obtained from a magnetisation-temperature measurement at the corresponding applied field) (b) magnetic hysteresis loops at 4.2 K and (c) J_C as a function of magnetic field at 4.2 K for the five binary Sn-In alloys.

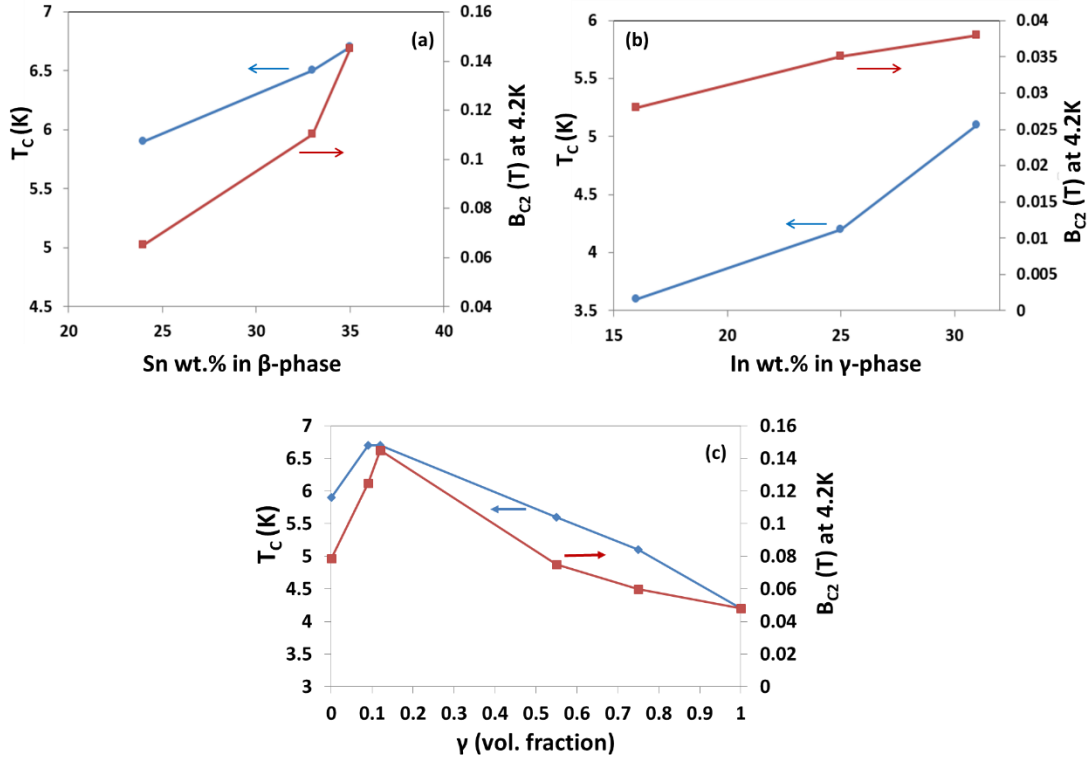


Figure 4: Superconducting properties (T_c and B_{c2} (4.2 K) values) as a function of solute concentration in (a) the β -phase (b) the γ -phase, (c) Superconducting properties as a function of volume fraction of the γ -phase in binary Sn-In alloys.

3.3.1. Quenching and ageing effects on the binary eutectic composition

As discussed above, the B_{c2} and J_c values of both the β -phase and γ -phase in binary In-Sn alloys increase with increasing solute content. However, as shown in the binary phase diagram in Figure 1, the equilibrium solid solubility decreases on cooling, particularly in the β phase. As a result, both the composition and volume fraction of each phase in the microstructure can be altered by changing the cooling rate. Moreover, in many low melting point solders, the chemical composition of the two phases and the length scale of the microstructure are highly sensitive to thermal history because of the high rates of solid-state diffusion, even at room temperature [20; 21]. To study the effect of cooling rate and ageing on the microstructure and superconducting properties, quenching from the melt has been carried out by immersion in liquid nitrogen, and the stability of the quenched sample was studied by measuring the superconducting properties at different time intervals after casting.

Figure 5 along with Table 2 presents the microstructure and properties of the near-eutectic sample B3 after air-cooling, quenching and ageing at room temperature for one week. As solid state diffusion is so fast in this system, the chemistry and phase fractions of the air-cooled alloy closely match the equilibrium room temperature values predicted from the phase diagram. The quenched alloy has a slightly higher T_C value than the air-cooled alloy, an enhancement in B_{C2} of about 70% and a dramatic improvement in J_C at 4.2 K. This can be explained by examining the differences in the alloy microstructure. Firstly, the air-cooled sample contains almost equal fraction of the Sn-rich γ phase and In-rich β phase, whereas in the quenched sample the majority phase is the In-rich β phase with composition In-38%Sn. Since the superconducting properties of the β phase are superior to the γ phase, this results in an improvement in both T_C and B_{C2} . Secondly, the β phase in the quenched alloy is supersaturated with Sn, as expected from the phase diagram. This also has the effect of enhancing B_{C2} , as discussed in previous section. The increase in T_C and B_{C2} are at least partly responsible for the improvement in J_C values.

In addition, the microstructure of the quenched alloy has a different morphology to the air-cooled sample, with the length of interphase boundary per unit area in the quenched sample being slightly higher than in the air-cooled sample because of the finer scale of the γ second phase. Since interphase boundaries can act as flux line pinning sites (discussed later in section 4), this modification in the morphology might also be responsible for the higher J_C values measured in the quenched sample. Therefore, the quench process improves the superconducting properties of sample B3 not only by altering the phase fractions and phase chemistry, but also by changing the scale of microstructure.

Table 2 also shows that the properties of the quenched sample change after one week at room temperature. B_{C2} and J_C values decrease significantly on ageing as a result of decreasing fraction of β phase, decreasing solute content of each phase and slightly lower boundary length.

A series of measurements taken over several days (given in Figure 6) showed that the J_C value dropped by about 30% in the first 7 days, before stabilising at this reduced value, as the microstructure evolves from that of the metastable quenched alloy towards the equilibrium room temperature microstructure.

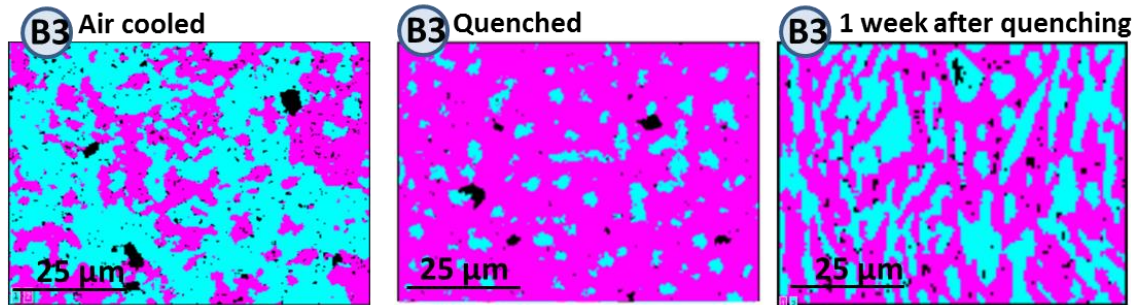


Figure 5: Phase maps of the Sn-In near-eutectic composition alloy (a) air cooled (b) quenched in liquid nitrogen, (c) 1 week after quenching at room temperature.

Table 2: Properties of sample B3 at different processing conditions; air-cooled, quenched and aged (one week after quenching).

Sample B3	Phases	Chemistry of the phases	T_c (K)	B_{c2} (T) at 4.2 K	J_c ($10^7 A/m^2$) at $T=4.2$ K, $B=0.01$ T	Boundary length per unit area ($\mu m/\mu m^2$)
Air-cooled	β (48%)+ γ (52%)	β :In78Sn22 γ :In32Sn68	5.6	0.04	3.1	0.35
Quenched	β (84%)+ γ (16%)	β :In62Sn38 γ :In33Sn67	6.7	0.145	12.2	0.41
1 week after quenching	β (60%)+ γ (40%)	β :In72Sn28 γ :In32Sn68	6.1	0.08	8.5	0.26

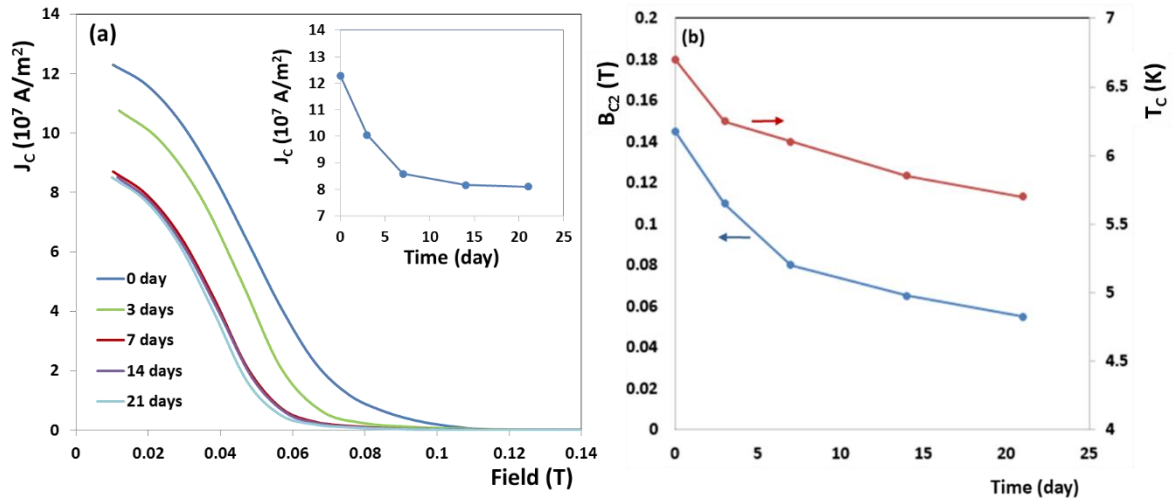


Figure 6: The ageing effects on the (a) J_c and (b) T_c and B_{c2} values of the quenched B3 (Sn-In near-eutectic composition).

3.2 Properties of the Sn-In-Bi ternary system

The ternary Sn-In-Bi system, in addition to the γ and β phases present in the binary Sn-In system, contains more superconducting phases, including BiIn and BiIn₂ with T_c values of 4.8K and 5.5K respectively [22]. We have studied this ternary alloy system to optimise both the microstructure and superconducting performance of potential new Pb-free solders.

3.2.1 Microstructural analysis

Figure 7 shows the compositions of the four ternary alloys studied in this work on the calculated ternary Sn-In-Bi phase diagram; T1 (Sn20In50Bi30), T2 (Sn50In30Bi20), T3 (Sn35In50Bi15) and T4 (Sn5In65Bi30), all in wt%. EDX phase maps of these alloys (air-cooled) are shown in Figure 8.

Sample T1 has a nominal composition of a ternary eutectic point in this system where it is expected that the molten alloy will solidify directly by the ternary eutectic reaction to γ , β and BiIn₂. The EDX phase map (Figure 8a) confirms the microstructure consists of the expected

phases, with the majority phase found to be BiIn_2 . The γ and β phases are formed close to each other within the BiIn_2 matrix. Similar microstructures have been previously reported for the eutectic composition in this ternary system [23; 24].

Sample T2, with an overall composition richer in Sn, has a two-phase microstructure consisting of BiIn distributed in a relatively fine scale within a matrix of the γ -phase. Sample T3 was chosen to engineer a microstructure with a majority of the β phase, as this phase has the best superconducting properties. EDX analysis confirms that this alloy contains β , γ and BiIn_2 phases, with the majority β phase forming a continuous matrix. The microstructure is significantly coarser in this sample than in the ternary eutectic (T1) which contains the same three phases in different volume fractions.

Sample T4 shows a two-phase microstructure of β and BiIn_2 , formed by a binary eutectic transition. There is no evidence of any γ phase, suggesting that for this starting composition solidification is complete before the ternary eutectic temperature is reached.

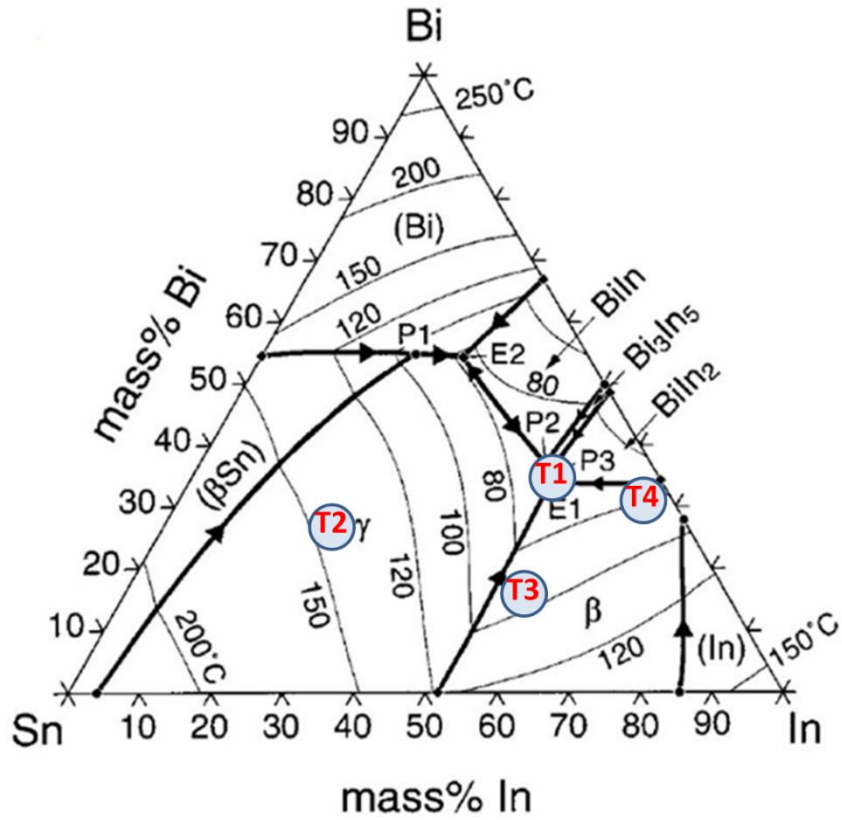


Figure 7: The calculated ternary Sn-In-Bi phase diagram [19] and the location of the four alloy compositions studied in this work.

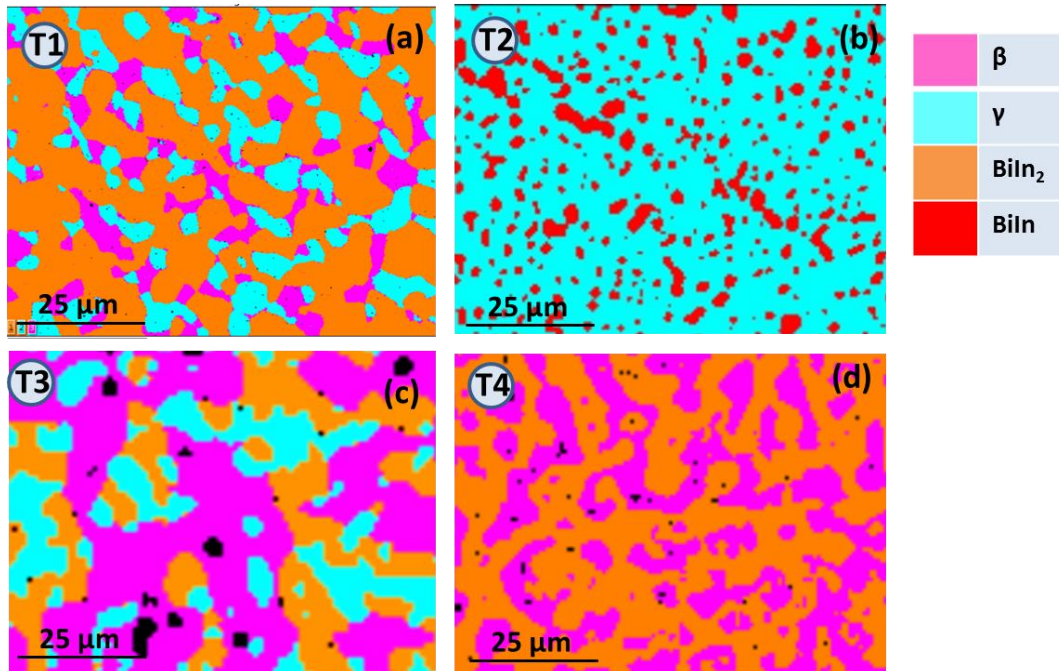


Figure 8: (a-d) Phase maps of the four studied ternary Sn-In-Bi alloys. Pink colour represents the β phase, blue the γ phase, orange BiIn_2 and red BiIn .

3.2.2. Superconducting properties

Superconducting properties of these ternary alloys are shown in Figure 9 and Table 3. Most of the alloys in the ternary Sn-In-Bi system that we have studied show better superconducting properties than those of the binary Sn-In alloys. The best superconducting properties were found to be 6.9 K, 0.18 T and 1.3×10^8 A/m² for T_C , B_{C2} (at 4.2K) and J_C (at 4.2K, 0.01T) respectively for sample T3. This is not a surprising result, as the main phase in this alloy is the β -phase with the best superconducting properties in this system. Moreover, as will be discussed later in section 4, the interphase boundaries are active pinning sites in these solders. Although sample T3 has a relatively coarse microstructure, and the lowest number for the boundary length per unit area compared to the other ternary alloys, it still shows the highest value of J_C (Figure 9b). This suggests that it is the intrinsically higher B_{C2} and T_C values of the β phase that are mainly responsible for the improved J_C values, and further suggesting that refinement of the microstructure to increase the interphase boundary length might result in enhancement of J_C by increasing pinning. This is supported by the fact that sample T2 has the second highest J_C value (at 4.2K) despite having relatively low T_C and B_{C2} values and. This J_C enhancement may be due to the high boundary length per unit area in this sample because in Figure 9b where J_C is plotted versus reduced field it is seen that T2 has higher J_C as a result of stronger pinning.

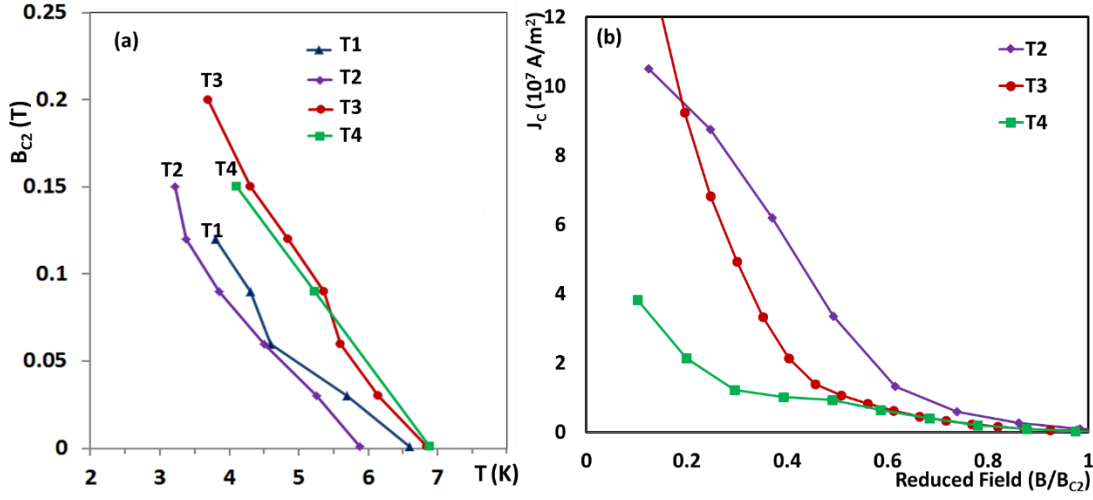


Figure 9: Superconducting properties of the air-cooled Sn-In-Bi alloys, (a) B_{c2} as a function of temperature, (b) J_c versus reduced field.

Table 3: Properties of the air-cooled Sn-In-Bi alloys studied in this work.

Sample	Majority phase	T_c (K) at 10 Oe	B_{c2} (T) at 4.2 K	J_c (10^7 A/m ²) at $T=4.2$ K, $B=0.01$ T	Boundary length per unit area ($\mu\text{m}/\mu\text{m}^2$)
T1	BiIn_2	6.6	0.09	0.003	0.32
T2	γ	5.9	0.075	10.5	0.4
T3	β	6.9	0.18	12.8	0.13
T4	$\beta+\text{BiIn}_2$	6.9	0.14	3.8	0.19

3.2.3. Quench and ageing effects in ternary alloys

The effects of quenching in liquid nitrogen from the melt and ageing on the microstructure and superconducting properties were also studied for samples T1, T3 and T4. As shown in Figure 10, quenching results in improved J_c values compared to the air-cooled samples for all of the alloys. However, this J_c enhancement is much larger for sample T1 at the ternary eutectic composition. As the phase maps show, the quenched microstructure still contains BiIn_2 as the

majority phase, but the secondary γ phase is distributed over the matrix in a very fine scale leading to high interphase boundary lengths per unit area. However, no β phase is detected in the quenched sample with the spatial resolution of the EDX mapping technique. Similarly, in sample T3, the quenched microstructure again only contains two phases. Quenching the T4 melt results in a significant refinement of the scale of the β phase.

The superconducting parameters and microstructure of these quenched samples were measured after one month to investigate the effect of room temperature ageing. As shown in Figure 10, microstructural coarsening occurs for all the samples, and J_C values notably decreases after one month for all of the samples. For example, in T3 which showed the best superconducting properties in these ternary Sn-In-Bi alloys, the J_C value decreases about 60%, a larger decrease than seen for the aged binary alloys. This is presumably due to the finer microstructure in the ternary alloys which provide more boundary length and so more fast diffusion paths to encourage coarsening. It can be concluded that the superconducting properties of both binary and ternary alloys can suffer from significant ageing at room temperature, and that this needs to be considered for the long-term reliability of joints made of these solders.

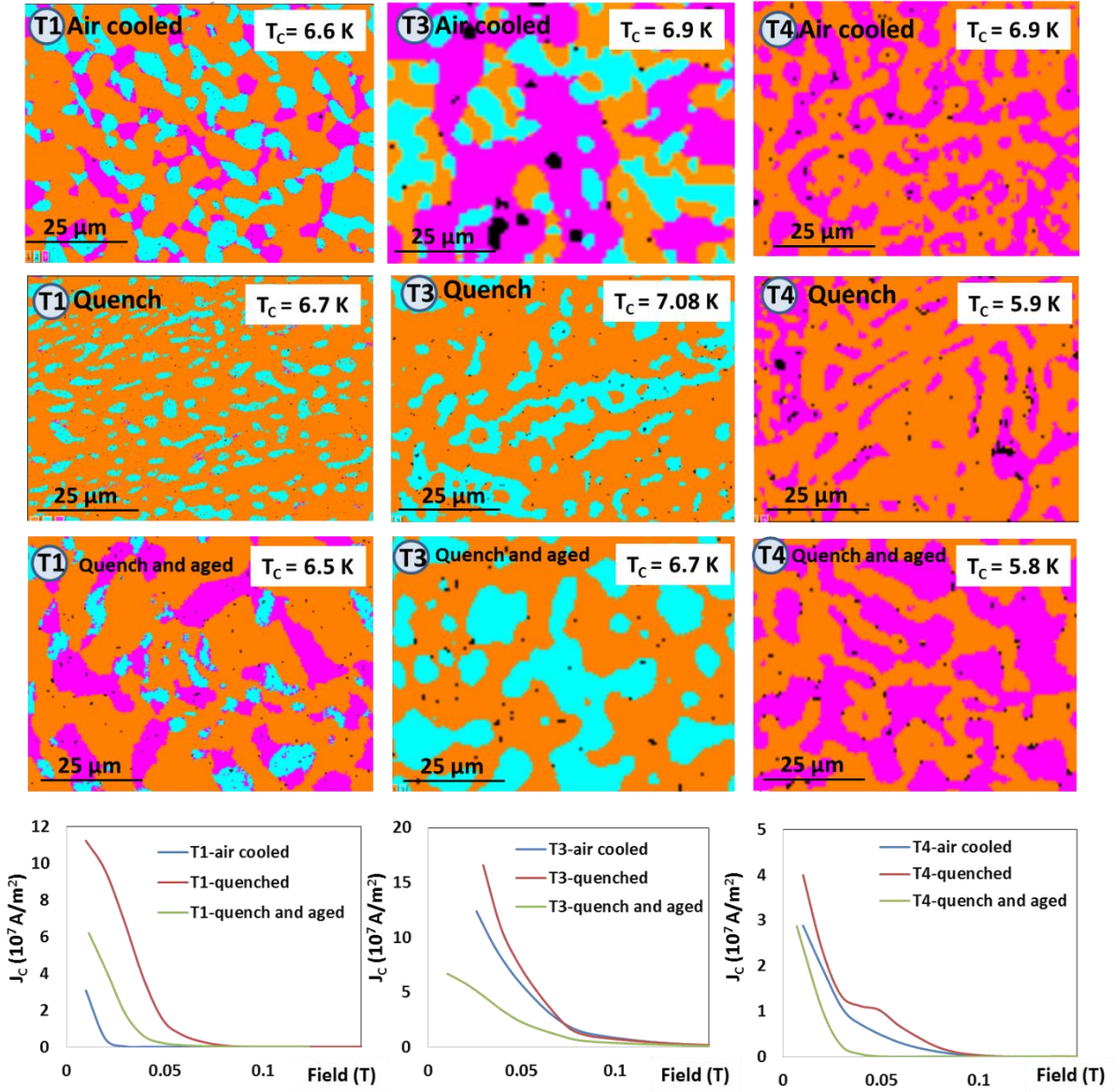


Figure 10: Microstructure and J_c as a function of magnetic field for samples T1, T3 and T4 (Air-cooled, Quenched and Aged for one month). Pink colour represents the β phase, blue the γ phase and orange BiIn_2 .

4. Pinning mechanisms

Since the critical current density of these solders will depend strongly on the pinning centres and the strength of these pinning sites, it is important to investigate the pinning mechanisms in these materials. To analyse the flux pinning strength and active pinning mechanisms, the Dew-Hughes model [17] and multi-elementary scaling modelling was employed.

According to the Dew-Hughes model [17], core pinning sites can arise from two phenomena, ‘ $\Delta\kappa$ pinning’ resulting from small differences in the Ginzburg parameter due to composition fluctuations, and ‘normal pinning’ resulting from non-superconducting particles such as normal phases and defects. Depending on the size of the pinning centres compared to the inter flux line spacing (d), the pinning sites can be defined as point, surface or volume pins. Point sites are regions with all dimensions less than d , surface sites have two dimensions greater than d and volume sites have all dimensions larger than d . Therefore, in the Dew-Hughes model, there are six pinning functions describing the core pinning sites defined using the following equation:

$$F_p = Ab^p(1-b)^q \quad \text{Eq. 1}$$

where ($b=B/B_{C2}$), F_p is the pinning force density, A is a parameter associated with the pinning strength and p and q are parameters describing the actual pinning mechanism. The theoretical values of p and q and the position of the peak maximum in the Kramer plot (F_p versus b) depend on the geometry (point, surface and volume) and the type (normal or $\Delta\kappa$) of the active pinning sites[17].

By fitting a curve to the experimental data, p and q values can be evaluated and the active pinning mechanisms can be identified. However, there may exist several active pinning mechanisms simultaneously with different contributions to the overall flux pinning. It is therefore more precise to consider all the mechanisms and give each of them a weighting parameter (A , B , C , D and E) in the equation of the fitted curve [18]:

$$F_p = Ab(1-b) + Bb^{0.5}(1-b)^2 + Cb^{1.5}(1-b) + Db(1-b)^2 + Eb^2(1-b) \quad \text{Eq. 2}$$

The weighting parameters which show the contribution of each mechanism can be determined by fitting a curve to the above equation. This method has been applied by several groups [18; 25-27].

Figure 11 shows the pinning force density (F_p/F_{max}) of the T3 (air-cooled) sample as a function of the reduced magnetic field (B/B_{C2}). The data shows a reasonably good fit of the scaling law considering all the pinning mechanisms. The weighting parameters (A,B,...E) obtained from this curve-fitting (inset of Figure 11) show that parameter B is much higher than the other weighting parameters suggesting that pinning is dominated by the *surface normal* mechanism. This is also supported by the observation that maximum value of F_p occurs at a reduced field value of about 0.2, as expected for the *surface normal* pinning mechanism. Similar curve-fitting analysis was carried out for all the air-cooled Sn-In and Sn-In-Bi solders studied in this work, and for all of these solders the dominant mechanism was found to be *surface normal* pinning. In these microstructures, the individual eutectic lamellae are always larger than the penetration depth of the superconducting phases, even at the fastest solidification rates, and cannot perform as effective volume pinning sites [20], but the interphase boundaries and grain boundaries have been reported to be effective surface (2D) pinning sites [6].

To evaluate the importance of all possible 2D boundaries (both grains and interphase boundaries), EBSD mapping was carried out for sample T3 (air-cooled). Figure 12 shows the EBSD maps of the grains and phases in this sample. Consistent with the phase maps obtained by EDX (Figure 8c), the EBSD phase map shows a similar phase pattern containing β , γ and BiIn_2 . However, the grain map shows a finer scale compared to the phase map, suggesting that many grain boundaries also exist in the sample contributing to the flux pinning. The grain map of each individual phase is shown in Figure 12c-e. It is seen that the grain size is larger in the BiIn_2 phase compared to the other two phases.

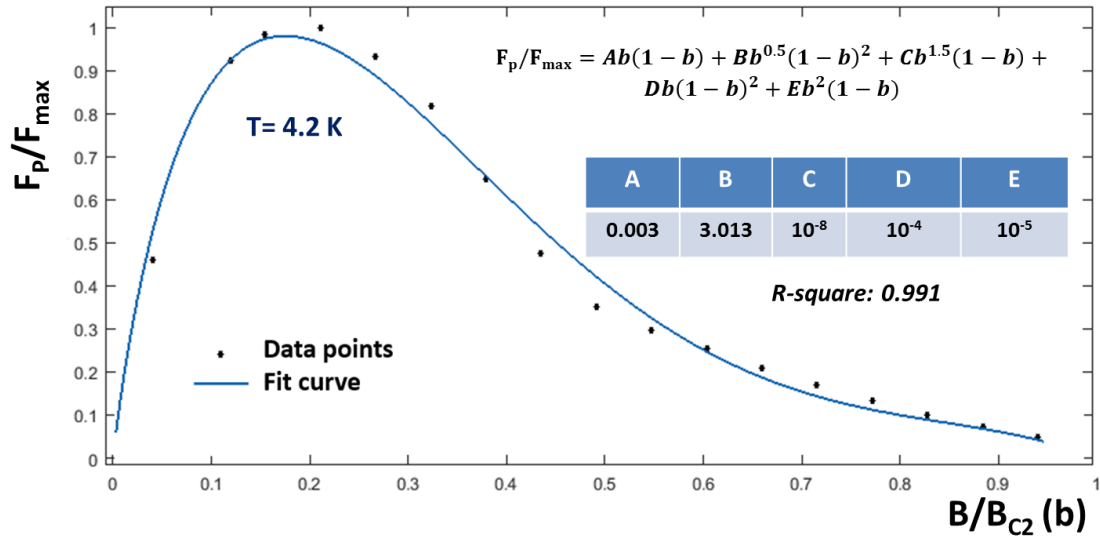


Figure 11: Normalised pinning force as a function of normalized magnetic field for the T3 solder, and the fitted curve considering all pinning mechanisms. The equation used for curve-fitting is shown in the inset with all the details of curve-fitting.

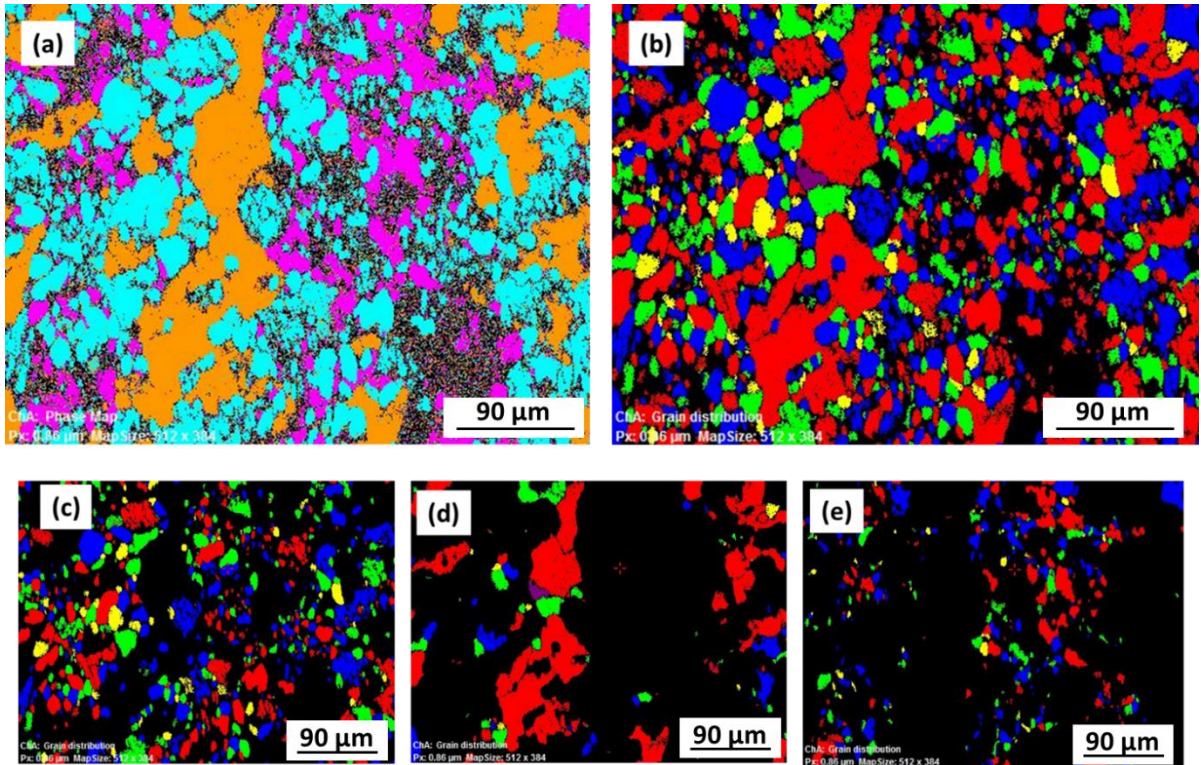


Figure 12: (a) EBSD phase map of ternary T3 sample after air cooling. Black pixels are regions where the EBSD pattern quality was poor as a result of porosity (mainly present in the β phase), (b) EBSD grain map of the same area (c, d and e) EBSD grain maps segmented for the γ , BiIn₂ and β

phases respectively. Small grains (less than 5 pixels in size) have been removed and different grains (defined with a 5° tolerance) are given arbitrary colours.

It was found that the cooling rate has an influence on the pinning force density in these solders. As seen in Figure 13, the pinning force density is higher for the T3 sample when quenched, whereas the pinning force considerably decreases after ageing. By referring to the microstructure in Figure 10, it can be suggested that in the quenched sample, due to the finer microstructure, the interphase boundary length per unit area is higher leading to an increase in the pinning force. Similarly, in the aged sample, the microstructure is coarsened because of the fast diffusion in these materials, leading to a lower density of boundaries and lower pinning force density. This shows that in these materials, pinning strength can be manipulated by the scale of the microstructure as well as by composition. It has been reported in the literature that the density of the interphase boundaries (ie the scale of the microstructure) in all binary solder alloys as well as some ternary alloys such as Sn-In-Bi [28] can be controlled by the solidification rate since the phase spacing (λ) and growth rate (R) are related by the well-known relationship for eutectic solidification $\lambda^2 R = \text{constant}$.

In Figure 13, it can also be seen that the position of the maximum F_p slightly changes in the quenched sample from $B/B_{C2}=0.2$ towards higher magnetic fields (as shown in the inset) indicating the introduction of other pinning mechanisms. After ageing, the peak position goes back to 0.2 which is the characteristic of the *surface normal* pinning mechanism. The weighting parameters obtained from curve-fitting shows that in the quenched sample, in addition to the dominant mechanism of *surface normal* pinning, there is a small contribution of about 15% for the *volume* $\Delta\kappa$ mechanism. This mechanism is generated by variations of T_C from region to region over distances larger than the flux-line spacing. This might result from local chemical fluctuations likely to exist in the quenched sample, whereas in the air-cooled and aged samples,

the compositions are more uniform. It is worth noting that in the quenched sample, the dominant pinning mechanism is still surface normal pinning with only a small contribution of the volume $\Delta\kappa$ pinning.

The pinning forces and scaling parameters for all the ternary solders studied in this work were calculated, and are listed in Table 4. The curve fitting for all these quenched materials gives a contribution from the $\Delta\kappa$ mechanism of between 5% (T4) and 15% (T3).

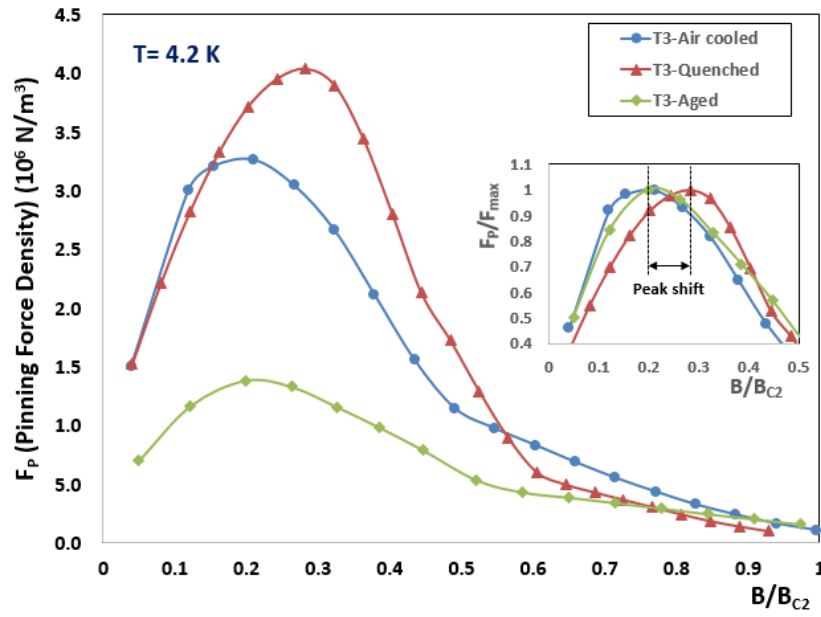


Figure 13: Pinning force density as a function of normalized field for sample T3 solidified at different cooling rates and aged at room temperature. The inset shows normalized pinning force density of these samples and the peak shift for the quenched T3 sample.

Table 4: Pinning force density and scaling parameters (according to Eq. 2) for all the ternary solders studied in this work.

Sample	Preparation condition	Pinning Force Density (10^6 N/m^3)	Scaling parameters	Boundary length per unit area ($\mu\text{m}/\mu\text{m}^2$)
T1	Air-cooled	1.3	B=1	0.32
	Quenched	3.1	B=0.9, A=0.1	0.51
	Aged	2.1	B=1	0.27
T3	Air-cooled	3.2	B=1	0.13
	Quenched	4.1	B=0.85, A=0.15	0.30
	Aged	1.3	B=1	0.21
T4	Air-cooled	1.5	B=1	0.19
	Quenched	1.6	B=0.95, A=0.05	0.33
	Aged	1.2	B=1	0.28

5. Conclusions

The microstructure and superconducting properties of binary Sn-In and ternary Sn-In-Bi alloys were studied to investigate the potential of these solders to replace the current industry standard Pb-based alloys. It was found that microstructural parameters such as phase chemistry, phase fraction and the scale of the microstructure all have a remarkable influence on the superconducting properties of these alloys. In both systems, the superconducting properties can be improved by increasing the volume fraction of the β phase. In the Sn-In system, superconducting properties of both β and γ phases are improved by increasing the solute content in solid solution. At high cooling rates, the phase chemistry and microstructure can be manipulated, leading to higher values of T_C , B_{C2} and J_C . However, the superconducting properties are also influenced by ageing at room temperature. A remarkable reduction in J_C and B_C values occurs soon after the samples are prepared, but these parameters become relatively stable.

The active pinning mechanism for these solders was found to be surface normal pinning. As a result, by increasing the density of grain boundaries/interphase boundaries (ie refinement of the microstructure), higher J_C can be achieved. Since the solidification rate strongly affects the scale of the eutectic microstructure, this is a possible way to control the superconducting properties of the solder, as long as a mechanism to limit the ageing effect can be found, for instance by pinning the interphase and grain boundaries with instable phases. For the quenched samples, in addition to the surface normal mechanism, there is a small contribution of the volume $\Delta\kappa$ mechanism as a result of chemical inhomogeneity in these samples.

In general, ternary Sn-In-Bi alloys show better superconducting properties compared to those of binary Sn-In alloys. The best values we have achieved in these systems are 6.9 K, 0.18 T and 1.3×10^8 A/m² for T_C , B_{C2} (at 4.2 K) and J_C (at 4.2 K, 0.01 T) respectively for the $\text{Sn}_{35}\text{In}_{50}\text{Bi}_{15}$ composition consisting of a majority phase β -phase in which fine fibers of γ and BiIn_2 are embedded. These J_C and B_C values are still well below those of Pb-based solders, and so that is still a considerable way to go to create a Pb-free replacement for the current standard solder materials for superconducting joints.

Acknowledgment

The authors would like to thank Mr G Brittles and Dr C Johnston for helpful discussions and Dr D Prabhakaran from the Clarendon laboratory for the use of MPMS.

References

- [1] R.F. Thornton, Superconducting joint for superconducting wires and coils, 1986.
- [2] C.A. Swenson, W.D. Markiewicz, IEEE Trans. Appl. Supercond. 9 (1999) 185-188.
- [3] S. Liu, X. Jiang, G. Chai, J. Chen, IEEE Trans. Appl. Supercond. 23 (2013) 4400504-4400504.

- [4] J. Cheng, J. Liu, Z. Ni, C. Cui, S. Chen, S. Song, L. Li, Y. Dai, Q. Wang, IEEE Trans. Appl. Supercond. 22 (2012) 4300205-4300205.
- [5] T. Fukuzaki, H. Maeda, S. Matsumoto, S. Nimori, S. Yokoyama, T. Kiyoshi, IEEE Trans. Appl. Supercond. 16 (2006) 1547-1549.
- [6] S.A. Levy, J. Appl. Phys. 37 (1966) 3659.
- [7] J.E. Evetts, J.M.A. Wade, J. Phys. Chem. Solids 31 (1970) 973-982.
- [8] W.H. Warren, Rev. Sci. Instrum. 40 (1969) 180.
- [9] M. Merriam, M. Von Herzen, Phys. Rev 131 (1963) 637-643.
- [10] G. Brittles, T. Mousavi, C. Aksoy, C. Grovenor, S. Speller, Superconducting Science and Technology 28 (2015) 093001.
- [11] K. Seo, S. Nishijima, K. Katagiri, T. Okada, IEEE Trans. Magn. 27 (1991) 1877-1880.
- [12] P. Priv. Comm. with Noonan.
- [13] Official Journal of the European Union, Directive 2011/65/EU (2011).
- [14] Official Journal of the European Union, Directive 2014/9/EU (2014).
- [15] C.P. Bean, Rev. Mod. Phys. 36 (1964) 31-39.
- [16] E.J. Kramer, Journal of Applied Physics 44 (1973) 1360-1370.
- [17] D. Dew-Hughes, Philosophical Magazine 30 (1974) 293-305.
- [18] M.H. Pu, Y. Feng, P.X. Zhang, L. Zhou, J.X. Wang, Physica C: Superconductivity 386 (2003) 47-51.
- [19] P. Villars, A. Prince, H. Okamoto, Handbook of ternary alloy phase diagrams, ASM International, 1995.
- [20] J.D. Livingston, J. Appl. Phys. 38 (1967) 2408.
- [21] C.H. Raeder, L.E. Felton, V.A. Tanzi, D.B. Knorr, Journal of Electronic Materials 23 (1994) 611-617.
- [22] L.I. Berger, B.W. Roberts, Properties of Superconductors, CRC Press, Boca Raton, 1997.
- [23] H. Kabassis, J.W. Rutter, W.C. Winegard, Metallurgical Transactions A 15 (1984) 1515-1517.
- [24] H. Kabassis, J. Rutter, W. Winegard, Materials Science and Technology 2 (1986) 985.
- [25] R. Ma, et al., Physica C: Superconductivity 411 (2004) 77-82.
- [26] M.H. Pu, Y. Feng, P.X. Zhang, L. Zhou, J.X. Wang, Y.P. Sun, J.J. Du, Physica C: Superconductivity 386 (2003) 41-46.
- [27] Y. Zhao, C. Ke, C.H. Cheng, Y. Feng, Y. Yang, P. Munroe, Physica C: Superconductivity 470 (2010) 1096-1099.
- [28] M.A. Ruggiero, J.W. Rutter, Materials Science and Technology Volume 13 (1997) 5.